© 2021 Wiley-VCH GmbH

NANO MICRO small

Supporting Information

for *Small,* DOI: 10.1002/smll.202007579

A Layer-by-Layer Assembly Route to Electroplated Fibril-Based 3D Porous Current Collectors for Energy Storage Devices

Seunghui Woo, Donghyeon Nam, Woojae Chang, Younji Ko, Seokmin Lee, Yongkwon Song, Bongjun Yeom, Jun Hyuk Moon, Seung Woo Lee, and Jinhan Cho**

WILEY-VCH

Supporting Information

A Layer-by-Layer Assembly Route to Electroplated Fibril-Based 3D Porous Current Collectors for Energy Storage Devices

Seunghui Woo[†], Donghyeon Nam[†], Woojae Chang[†], Younji Ko, Seokmin Lee, Yongkwon Song, Bongjun Yeom, Jun Hyuk Moon, Seung Woo Lee*, and Jinhan Cho*

[†]These authors equally contributed to this work.

*Corresponding authors

Contents

Characterization

FT-IR spectra of the multilayers were obtained using a CARY 600 spectrometer (Agilent Technology) in specular mode with a resolution of 4 cm^{-1}, and the collected data were plotted with spectrum analysis software (OMNIC, Nicolet). FE-SEM and EDS data were obtained using an S-4800 instrument (Hitachi). Transmission electron microscopy (TEM) data of synthesized NPs were obtained using a Tecnai 20 instrument (FEI). UV-vis spectra of the LbL-assembled multilayer on quartz glass slides were analyzed using a Lambda 35 instrument (Perkin Elmer) within a scan range of 200 – 800 nm. The quantitative deposition of multilayers was monitored through a quartz crystal microbalance QCM (QCM 200, SRS). The mass loading of each layer was converted from the QCM frequency change using the Sauerbrey equation.[S1] The electrical conductivity of the

electrode was monitored by four-probe measurement. The temperature dependence of the electrical conductivity of LbL-assembled Au NP-coated paper and Ni-EPs was measured using a physical property measurement system (PPMS-9, Quantum Design) over a temperature range from 2 to 300 K.

Electrochemical Measurements

The electrochemical investigation for all electrodes was conducted in a three-electrode configuration through an Ivium-n-stat (Ivium Technologies). The Ag/AgCl (3 M NaCl) electrode, Pt coil electrode, and pseudocapacitive NP/Ni-EP (active area of 1 cm^2) were used as the reference, counter, and working electrodes, respectively in 0.5 M Na_2SO_4 electrolyte. CV and GCD measurements were all investigated in the potential range of 0 V to 1 V. EIS measurements were performed in the frequency range of 100 kHz to 0.1 Hz with a perturbation amplitude of 0.01 V.

The electrochemical capacitance of the MnO/Ni-EP electrode was calculated with the following equations.[S2]

$$\text{Specific capacitance (C)} = \frac{\int i(V)dV}{2v\Delta VS} \quad \text{(for CV)} \qquad (1)$$

$$\text{Specific capacitance (C)} = \frac{I\Delta t}{\Delta V} \quad \text{(for galvanostatic charge/discharge measurements)} \qquad (2)$$

where $i, v, \Delta V, I,$ and Δt represent the current, scan rate (mV s^{-1}), operating voltage window (potential range), applied current density, and discharge time, respectively. The variable *S* in Eq. (1) indicates the active area of the electrode or mass of the active material.

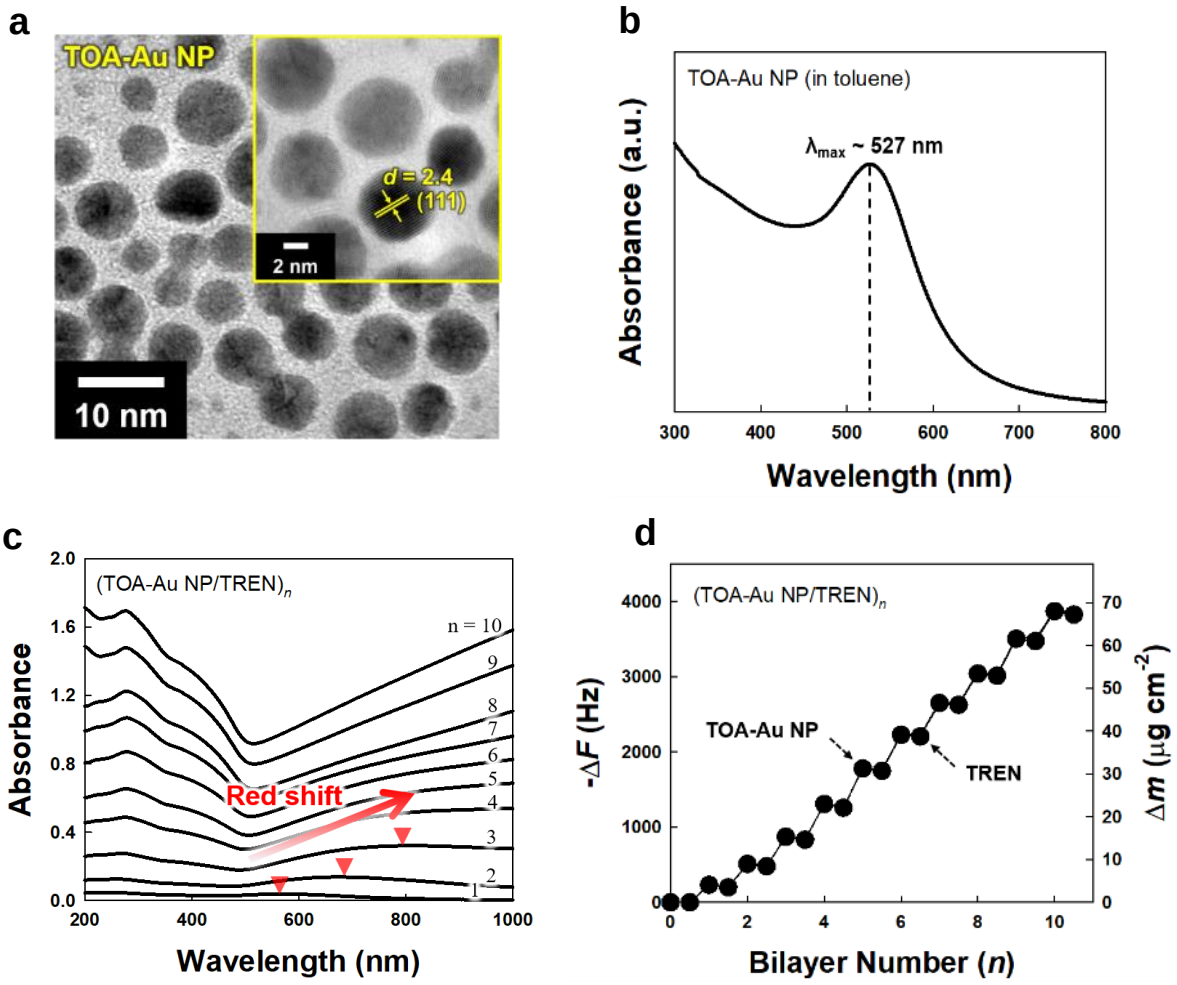

Figure S1. a) HR-TEM images of TOA-Au NP with a diameter of approximately 8 nm. b) UV-Vis spectra of TOA-Au NP in toluene. The TOA-Au NP in toluene exhibits the Surface resonance absorption peak at 527 nm. c) UV-Vis spectra of $(TOA\text{-}Au\ NP/TREN)_n$ multilayers as a function of the bilayer number (n). In this case, the absorption peaks of surface plasmon resonance spectra were strongly red-shifted with increasing the bilayer number (n) of $(TOA\text{-}Au\ NP/TREN)_n$ multilayers. d) QCM data for the $(TOA\text{-}Au\ NP/TREN)_n$ multilayer films as a function of the bilayer number (n).

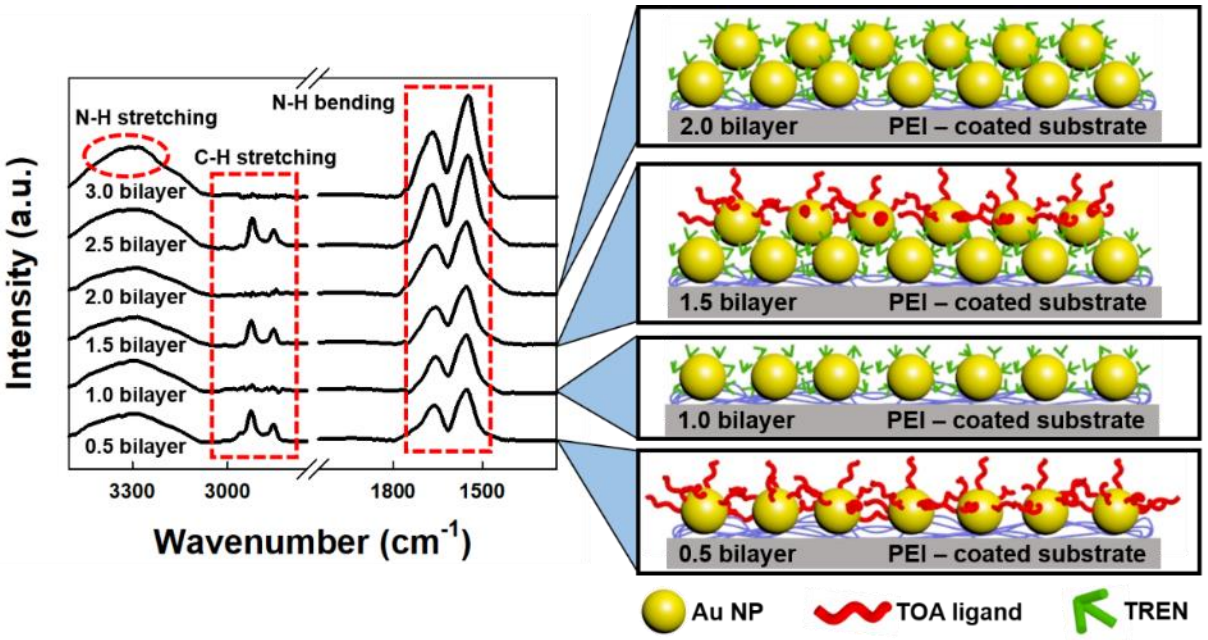

Figure S2. Fourier transform infrared (FT-IR) spectra and schematic illustration of the (TOA-Au NP/TREN)$_n$ multilayer films as a function of the bilayer number (n). As shown in the FT-IR spectra, the deposition of TOA-Au NP onto the poly(ethylene imine) (PEI)–coated Si substrate generated C-H stretching peaks from the long alkyl chains of TOA ligands at 2850 ~ 2950 cm^{-1} (herein, PEI containing large amounts of amine groups have a high affinity to the bare surface of Au NPs). When TREN was further deposited onto the outermost TOA-Au NP layer, the C-H stretching peaks disappeared, while the N-H bending peaks at 1550 ~ 1650 cm^{-1} and N-H stretching peaks at 3300 – 3500 cm^{-1} gradually increased. Therefore, the alternating deposition of TOA-Au NP and TREN repeated the generation and disappearance of the C-H stretching peaks originating from the TOA ligands when the outermost layer was changed from TOA-Au NP to TREN and vice versa.

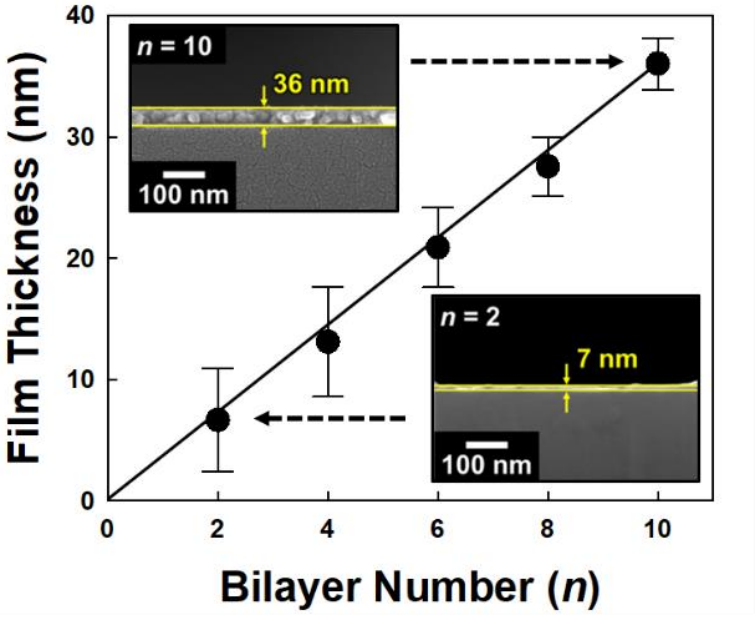

Figure S3. Thicknesses of the (TOA-Au NP/TREN)$_n$ multilayer films as a function of the bilayer number (*n*). The inset show the FE-SEM image of TOA-Au NP/TREN)$_{n=2 \text{ and } 10}$ multilayer films. In this case, the adsorption times of TOA-Au NPs in toluene and TREN in ethanol were 30 and 10 min, respectively. In this case, the thickness per bilayer was measured to be approximately 4 nm. Although the bilayer thickness is much thinner than the diameter of the individual TOA-Au NPs, subsequent depositions filled in the areas with insufficient surface coverage originating from sub-monolayer adsorption.

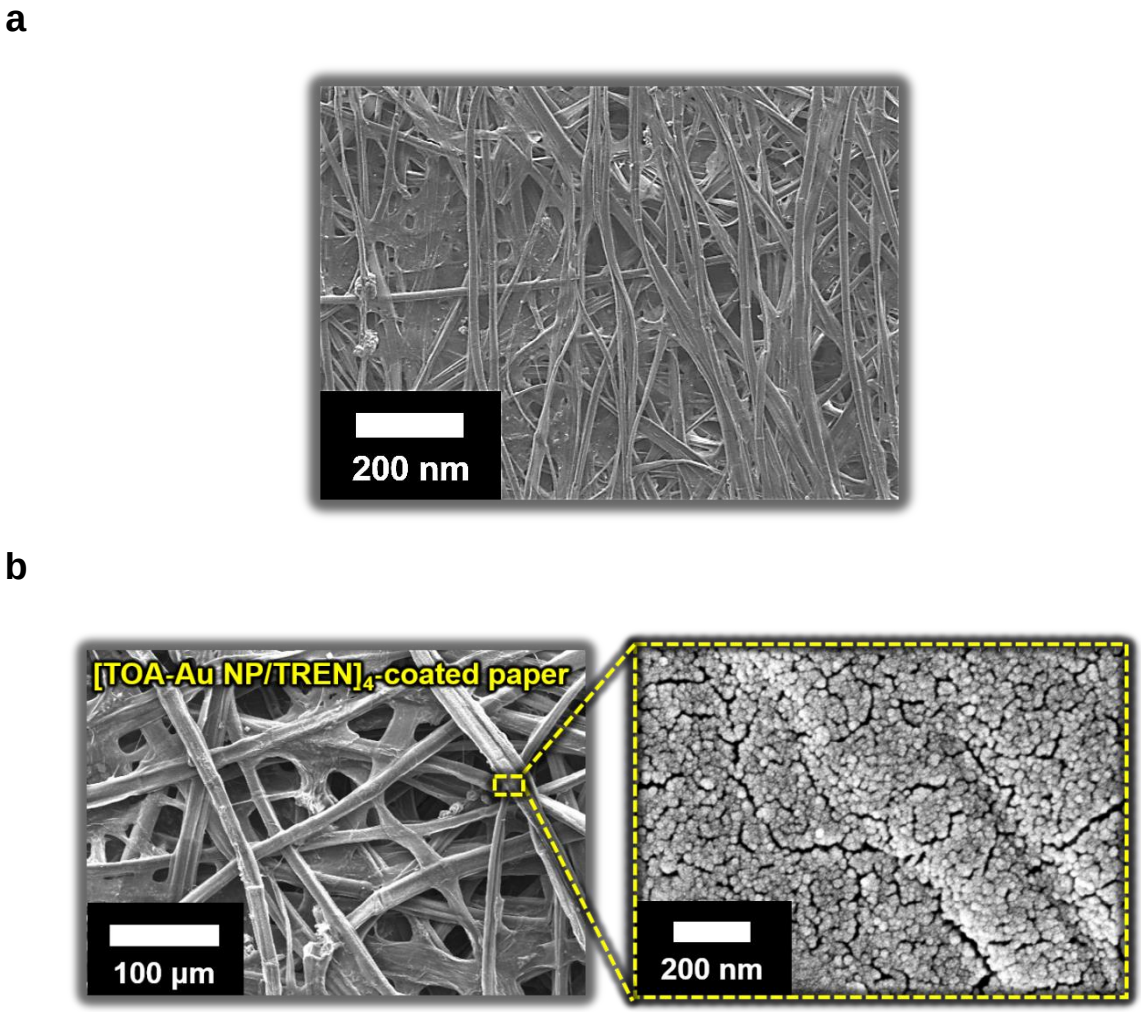

Figure S4. FE-SEM images of a) bare paper and b) (TOA-Au NP/TREN)$_4$ multilayer-coated paper.

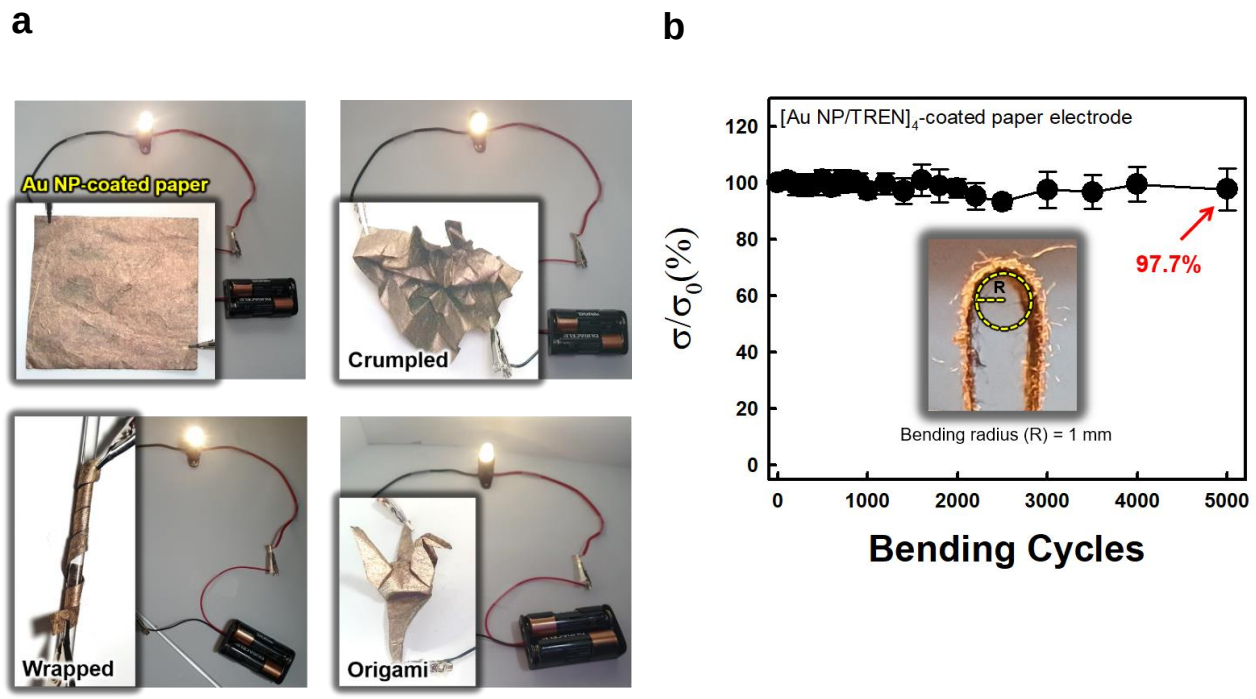

Figure S5. a) Photographic images of (TOA-Au NP/TREN)$_4$-coated paper electrodes with LED connection under crumpled, wrapped, and origami states. b) Relative electrical conductivity of (TOA-Au NP/TREN)$_4$-coated paper as a function of bending cycles.

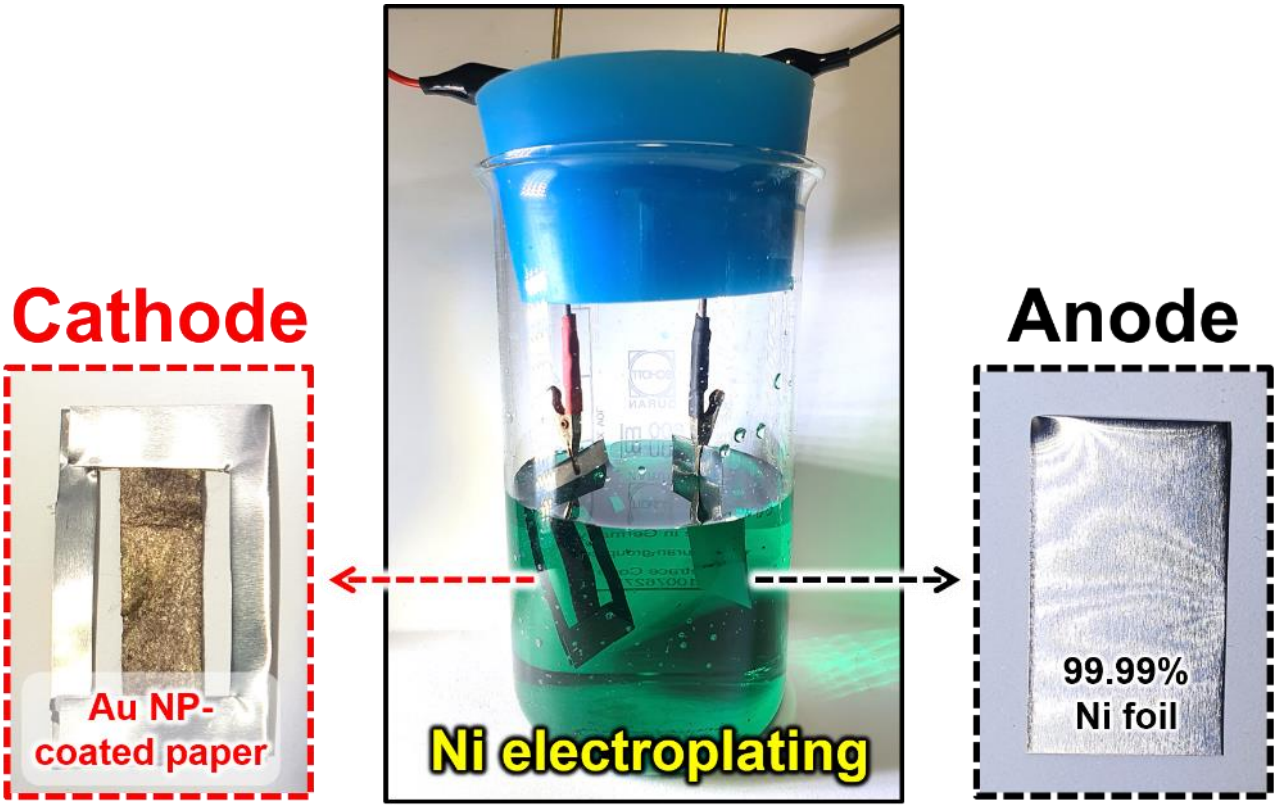

Figure S6. Photographic image of two-electrode configuration-based Ni electroplating setup. Au NP-coated paper was connected to the circuit as a cathode after being framed with Ni plate and 99.99% Ni foil was connected as an anode.

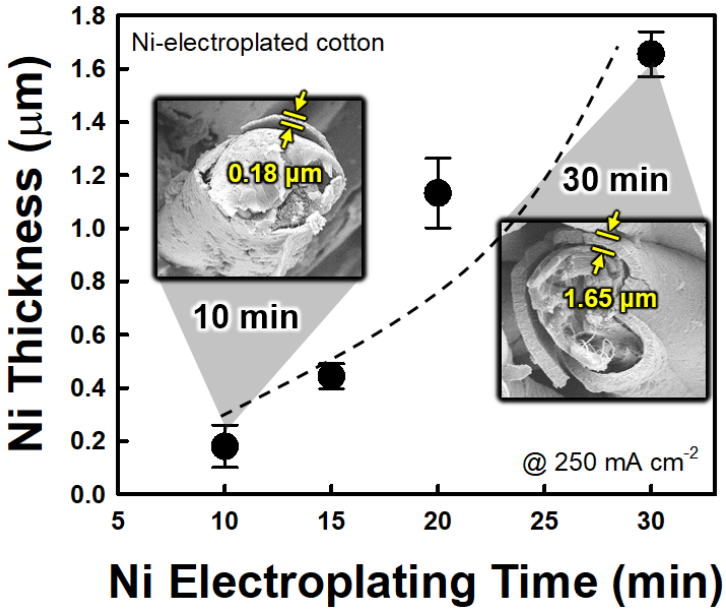

Figure S7. Thickness of electroplated Ni layer onto $(TOA\text{-}Au\ NP/TREN)_4$-coated cotton as a function of electroplating time at the fixed current density of 250 mA cm^{-2}.

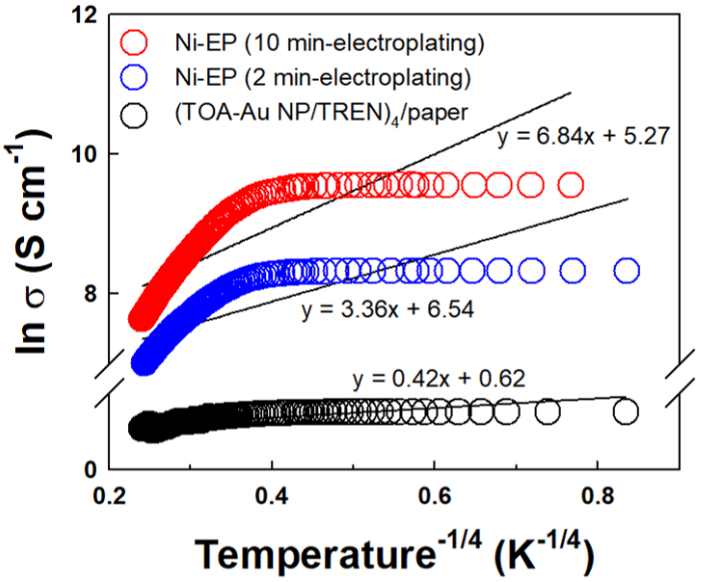

Figure S8. Plots of the conductivity (lnσ) vs. temperature ($K^{-1/4}$) for $(TOA\text{-}Au\ NP/TREN)_4$-paper and Ni-EPs (electroplating time = 2 and 10 min).

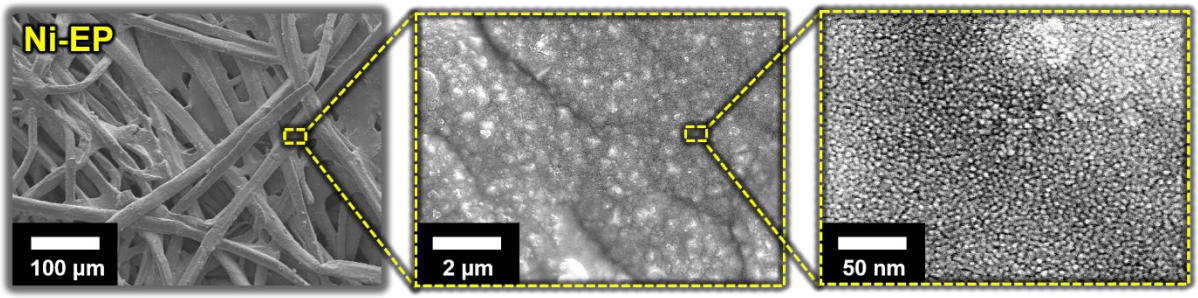

Figure S9. FE-SEM image of Ni-EP (i.e., electroplated Ni/(TOA-Au NP/TREN)$_4$-coated paper).

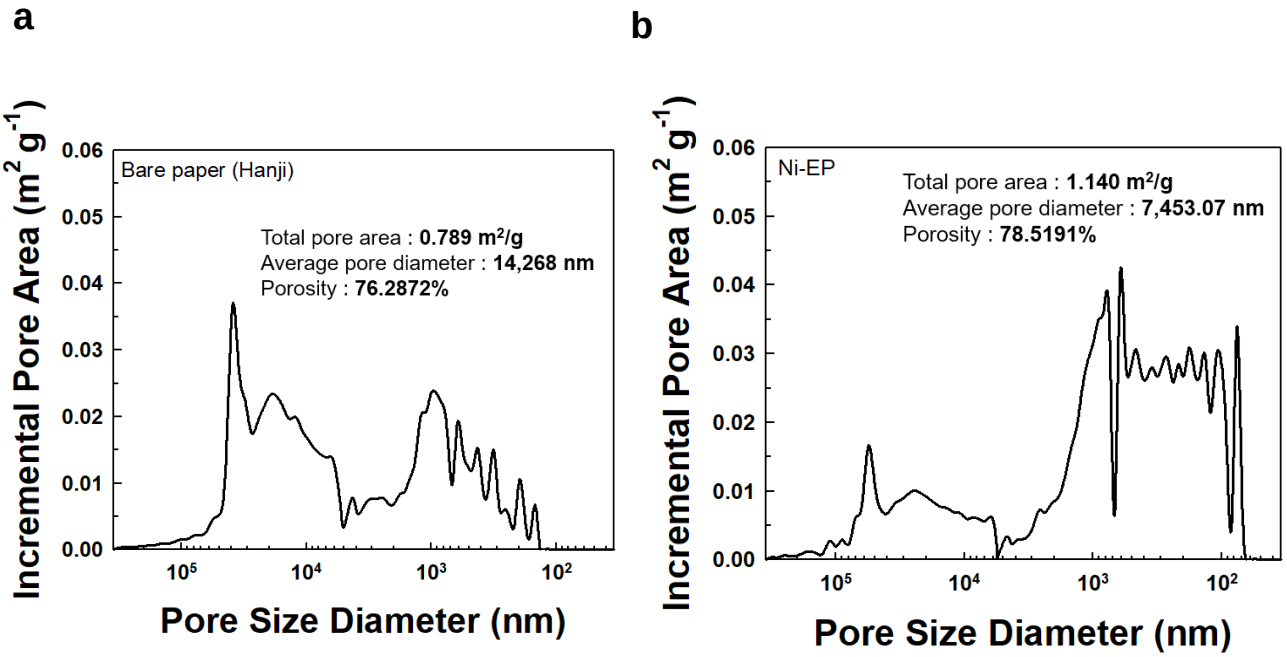

Figure S10. Incremental intrusion area of mercury versus pore diameter for a) bare paper an d b) Ni–EP using mercury porosimetry technique.

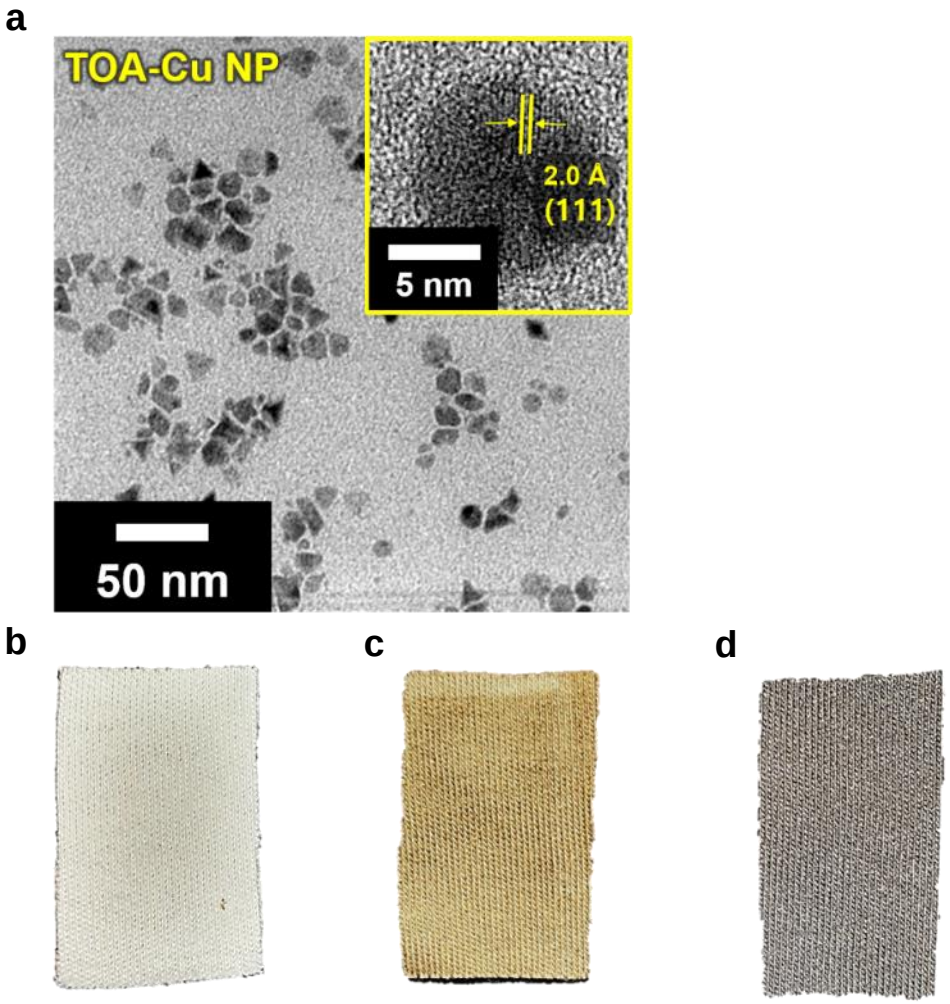

Figure S11. a) HR-TEM images of TOA-Cu NP with a diameter of approximately 8.5 nm. Photographic images of b) bare, c) Cu NP-coated, and d) Ni-electroplated cotton.

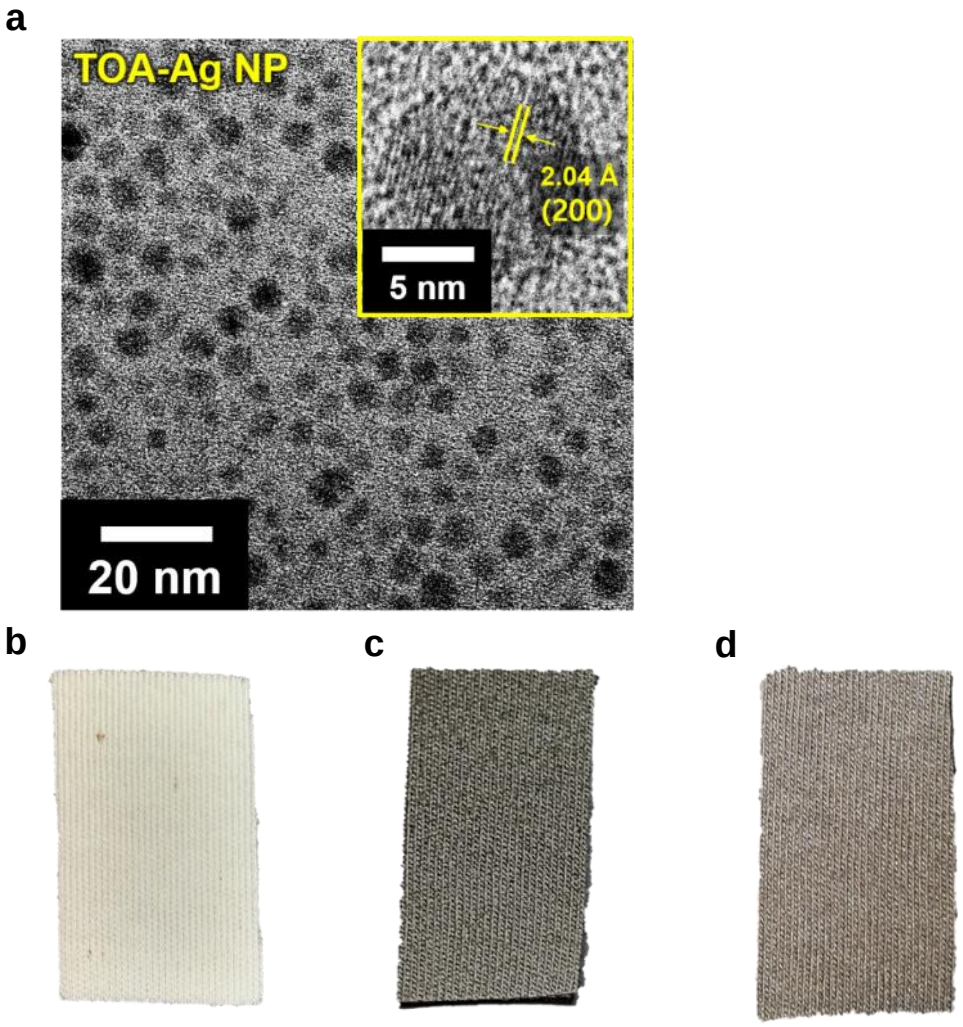

Figure S12. a) HR-TEM image of TOA-Ag NP with a diameter of approximately 8 nm. Photographic images of b) bare, c) Ag NP-coated, and d) Ni-electroplated cotton.

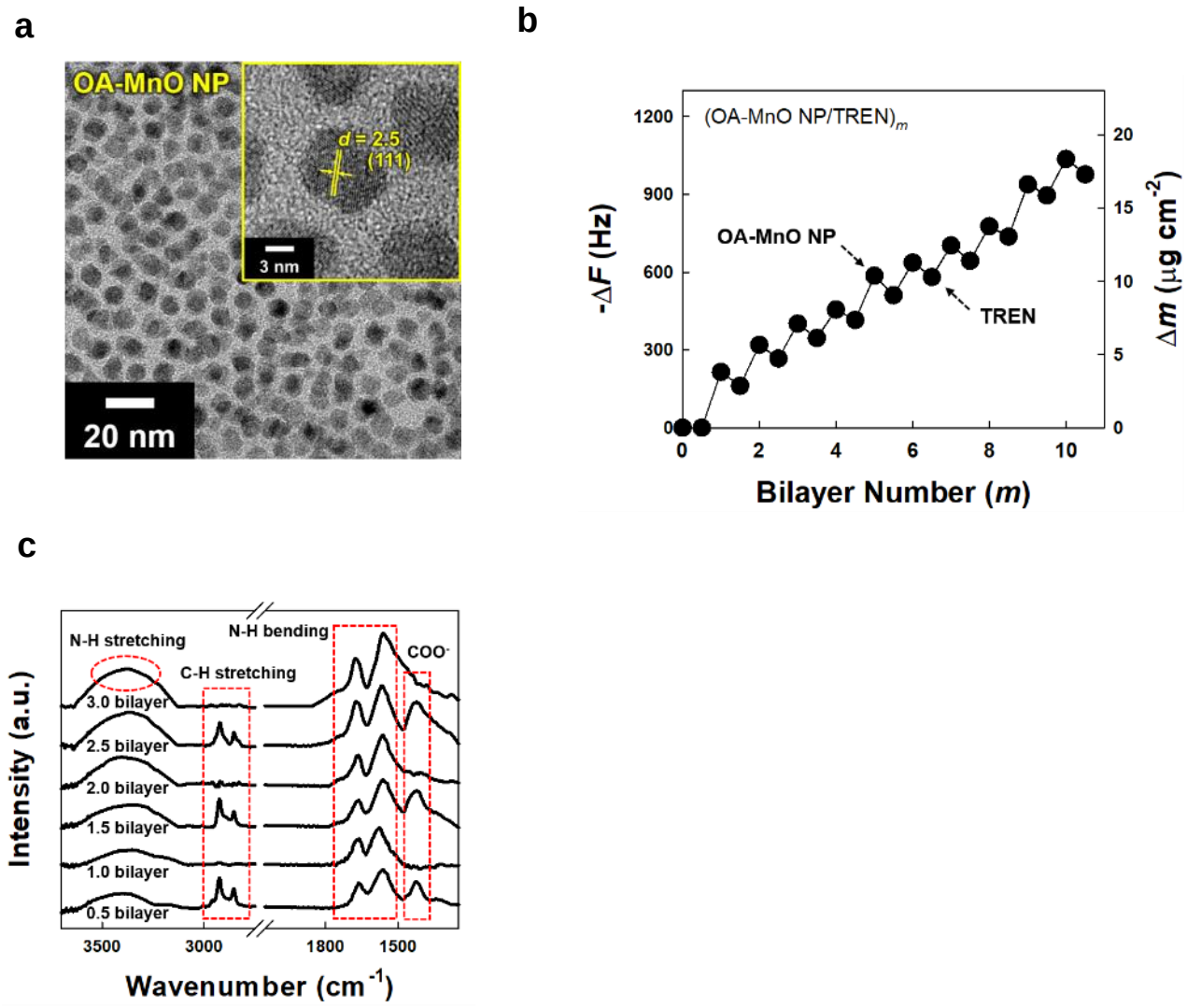

Figure S13. a) HR-TEM images of OA-MnO NPs. b) QCM data of the (OA-MnO NP/TREN)$_m$ multilayer films as a function of the bilayer number (m). c) FT-IR spectra of the (OA-MnO NP/TREN)$_m$ multilayer films with increasing bilayer number (m). As mentioned earlier (see **Figure S2**), the generation and disappearance of the C-H stretching peaks (from the long alkyl chains of OA ligands at 2850 – 2950 cm^{-1}) were repeated through the ligand-exchange reaction between OA ligands and TREN. Additionally, the N-H bending peaks at 1550 – 1650 cm^{-1} and N-H stretching peaks at 3300 – 3500 cm^{-1} gradually increased. The change of COO^- stretching peak of OA ligands was monitored at 1420 cm^{-1} because of the overlap of the COO^- stretching peak at 1520 cm^{-1} with N-H bending peaks.

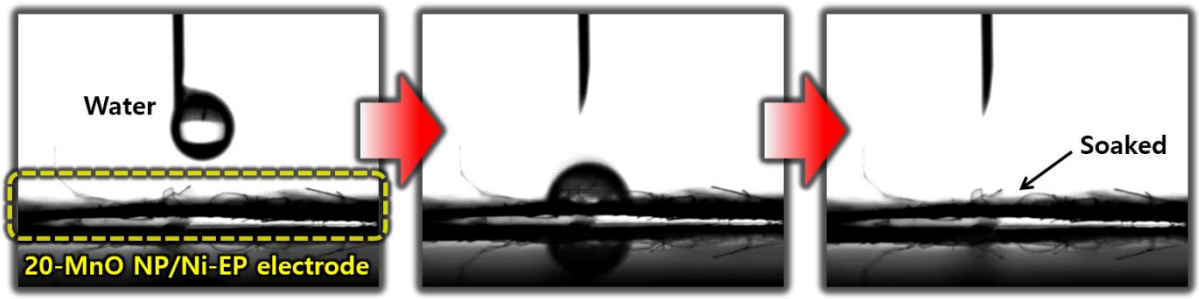

Figure S14. Photographic images of the water droplets on the 20-MnO NP/Ni-EP electrode over a short period of time.

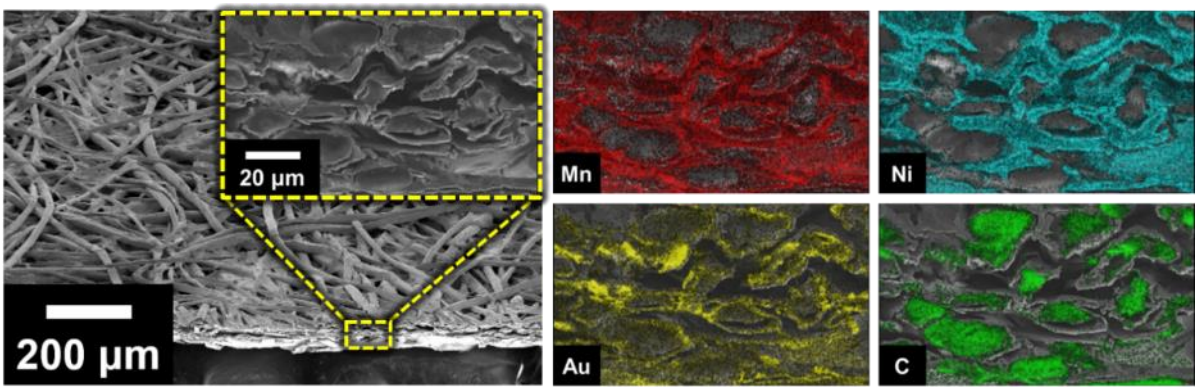

Figure S15. Tilted FE-SEM and EDS mapping images of 20-MnO NP/Ni-EP.

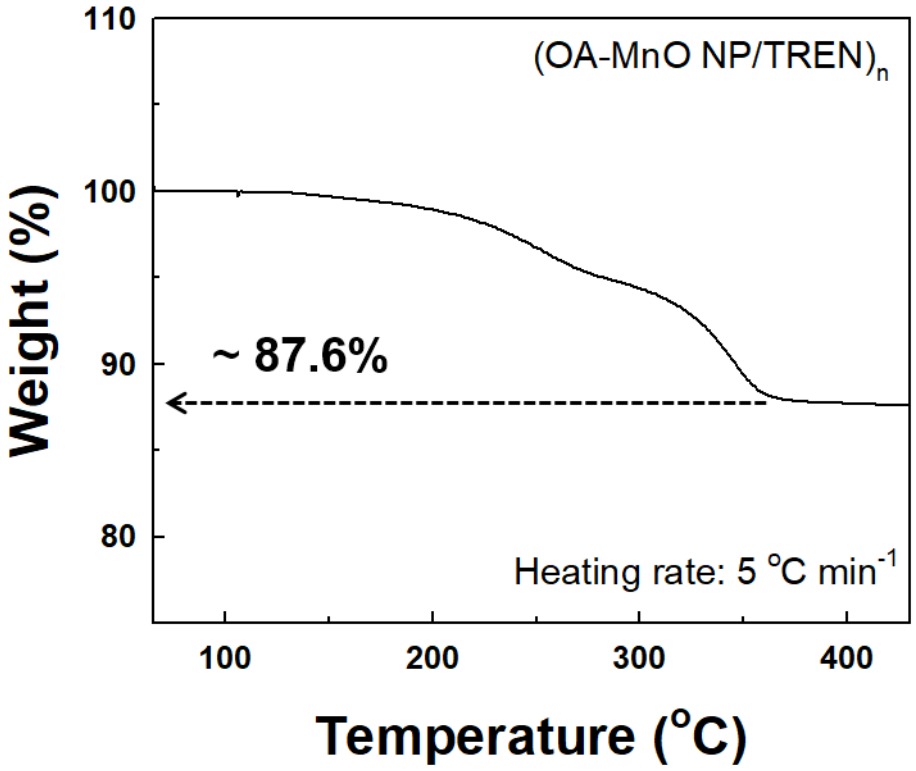

Figure S16. TGA data of $(OA\text{-}MnO\ NP/TREN)_n$ nanocomposite multilayers.

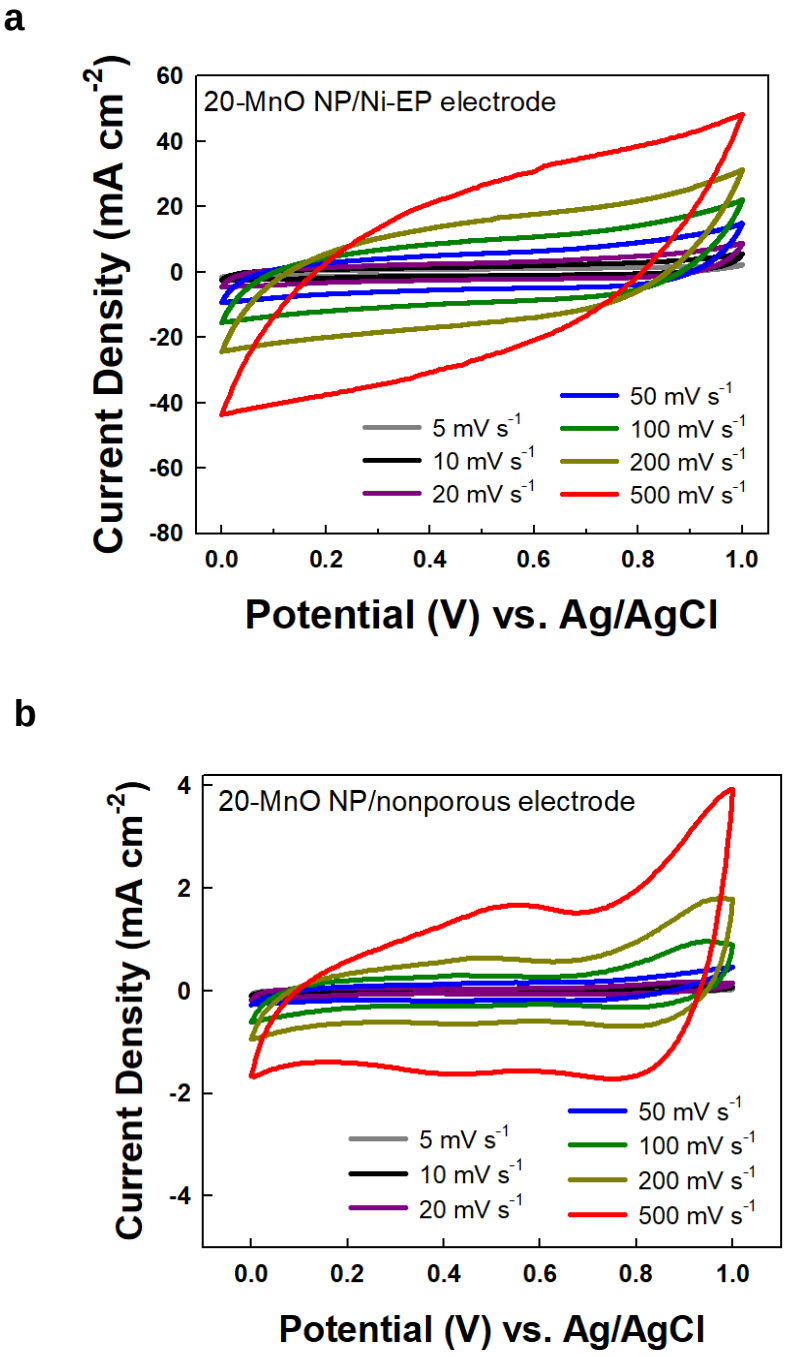

Figure S17. a) CVs of the 20-MnO NP/Ni-EP electrode as a function of scan rate. b) CVs of the 20-MnO NP/nonporous electrode as a function of scan rate.

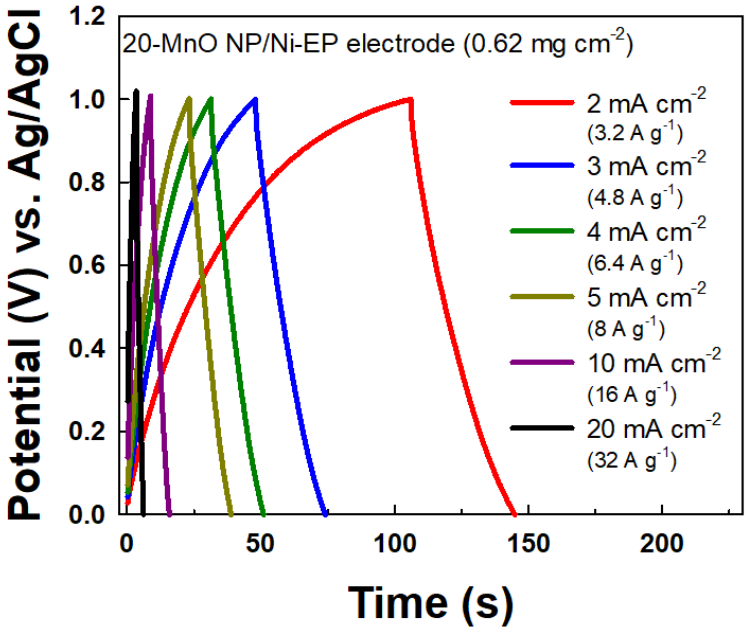

Figure S18. Galvanostatic charge/discharge (GCD) curves of the 20-MnO NP/Ni-EP electrode at various current densities in the range of 2–20 mA cm^{-2} (3.2–32 A g^{-1}).

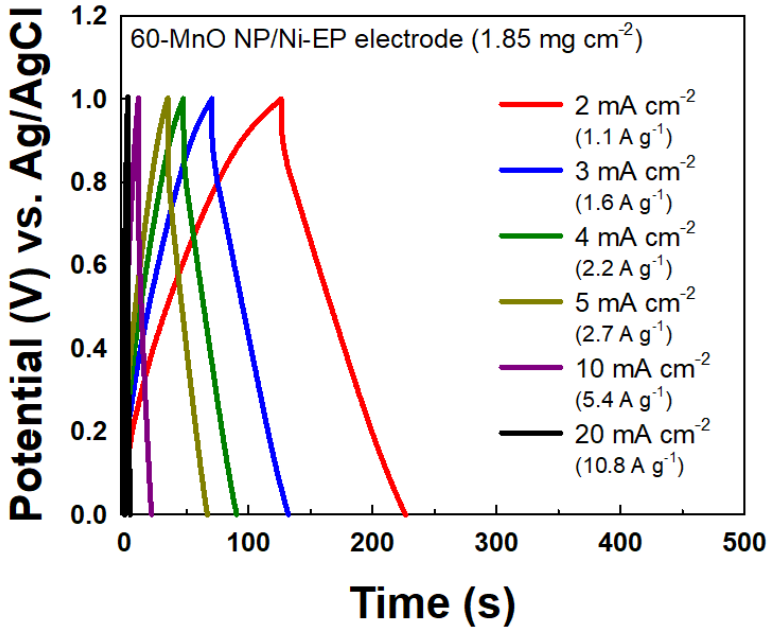

Figure S19. Galvanostatic charge/discharge (GCD) curves of the 60-MnO NP/Ni-EP electrode at various current densities in the range of 2–20 mA cm^{-2} (1.1–10.8 A g^{-1}).

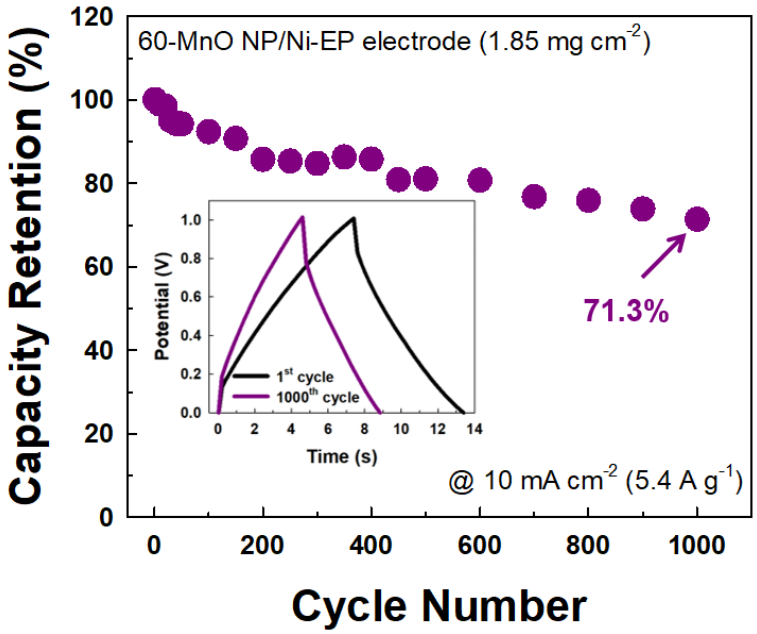

Figure S20. Cycling retention of the 60-MnO NP/Ni-EP electrode at 10 mA cm^{-2} (5.4 A g^{-1}). The inset shows the GCD curves measured after 1st and 1000th cycles.

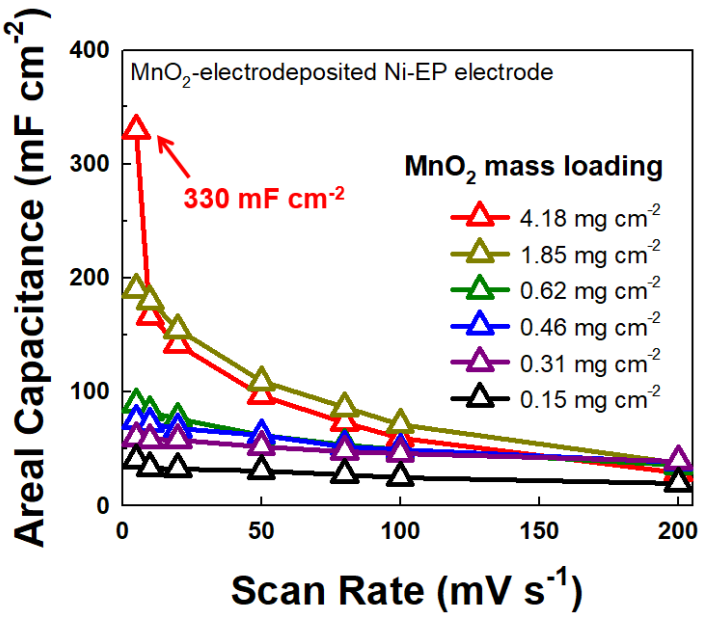

Figure S21. Areal capacitances of electrodeposited MnO_2-based Ni-EP electrodes with various mass loading densities. In the case of MnO_2-electrodeposited Ni-EP electrode with a mass loading of 4.18 mg cm^{-2} (for electrodeposited MnO_2), its loading mass was similar to that of 140-MnO NP/Ni-EP electrode (mass loading of LbL-assembled MnO NPs ~ 4.18 mg cm^{-2}).

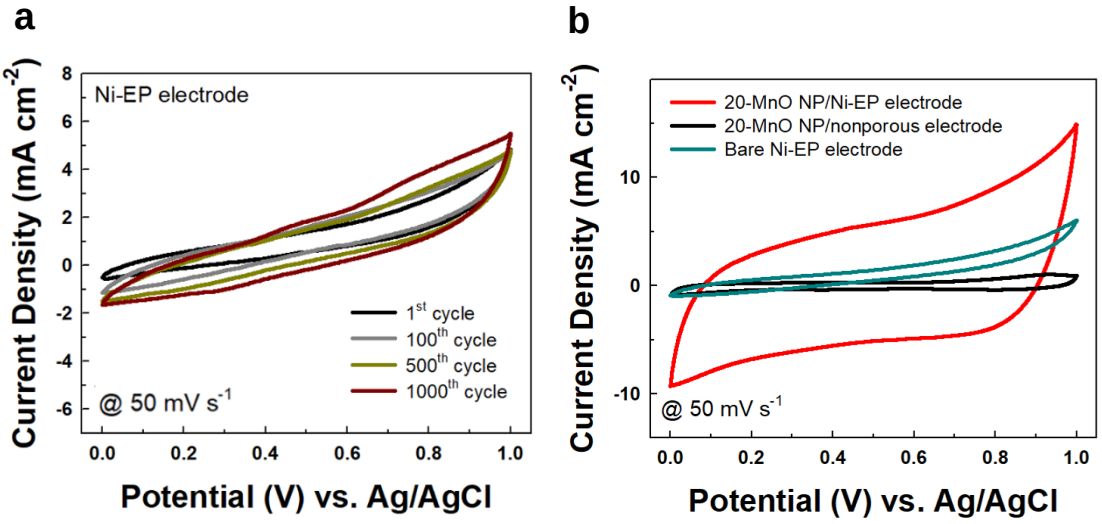

Figure S22. a) CV curves of bare Ni-EP current collector number at a scan rate of 50 mV s^{-1} as a function of cycling number. b) CV curves of the 20-MnO NP/Ni-EP electrode, 20-MnO NP/nonporous electrode, and bare Ni-EP electrode at a scan rate of 50 mV s^{-1} (for convenience, Figure 5c is re-used)

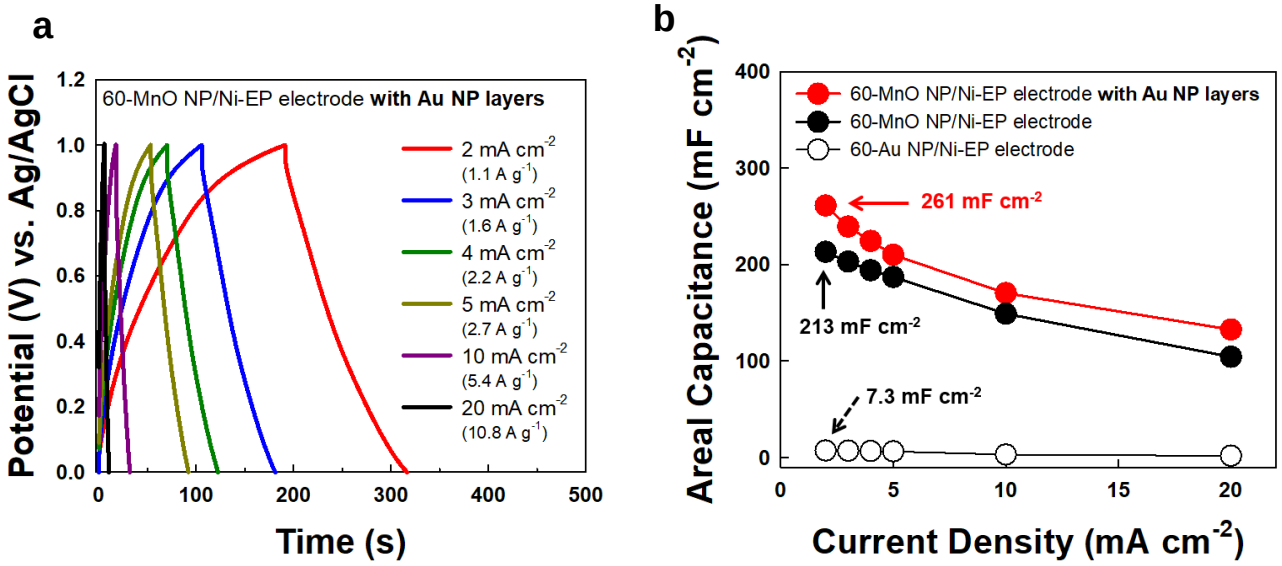

Figure S23. a) GCD curves of the 60-MnO NP/Ni-EP electrode with Au NP layers at various current densities in the range of 2–20 mA cm^{-2} (1.1–10.8 A g^{-1}). b) Areal capacitances of 60-MnO NP/Ni-EP electrode with Au NP layers, 60-MnO NP/Ni-EP electrode, and 60-Au NP/Ni-EP electrode as a function of current densities (2-20 mA cm^{-2}).

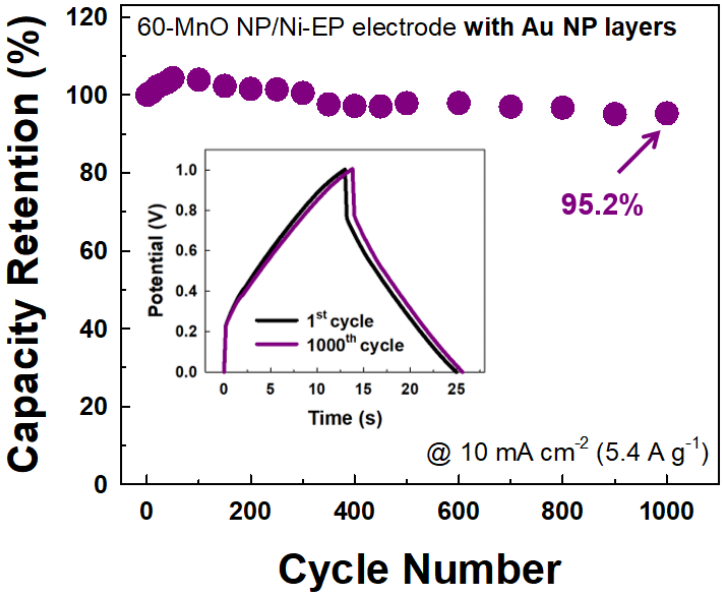

Figure S24. Cycling retention of the 60-MnO NP/Ni-EP electrode with Au NP layers at 10 mA cm^{-2} (5.4 A g^{-1}). The inset shows the GCD curves measured after 1st and 1000th cycles.

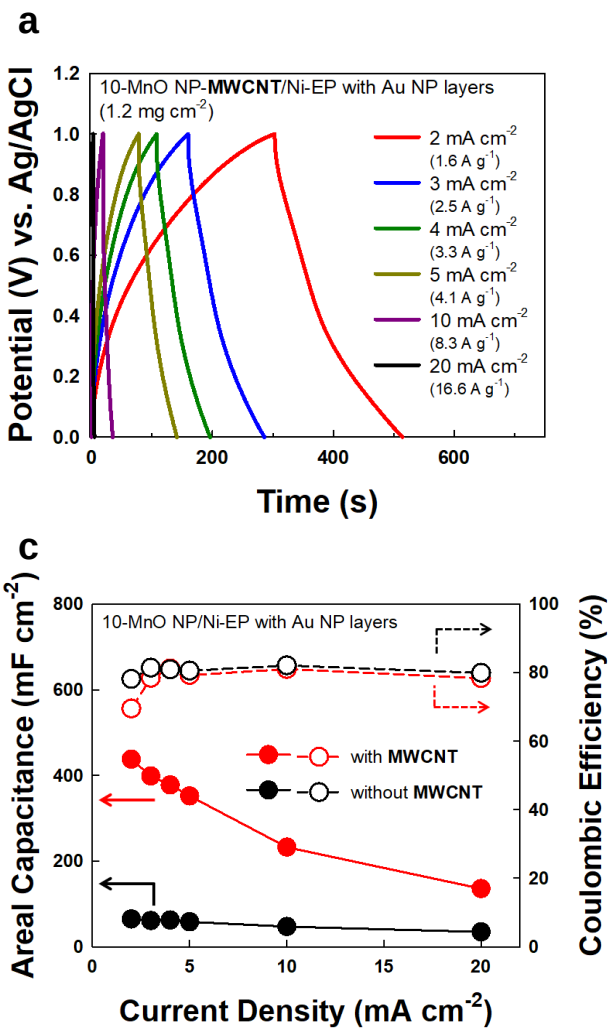

Figure S25. GCD curves of a) $(MnO\ NP/TREN)_{10}/(COOH\text{-}MWCNT/TREN)_{10}$ multilayer-coated Ni-EP electrode (i.e., 10-MnO NP-MWCNT/Ni-EP) with Au NP layers and b) 10-MnO NP/Ni-EP electrode with Au NP layers. c) Areal capacitance and Coulombic efficiencies of 10-MnO NP-MWCNT/Ni-EP with Au NP layers and 10-MnO NP/Ni-EP with Au NP layers at various current densities in the range of 2–20 mA cm^{-2}.

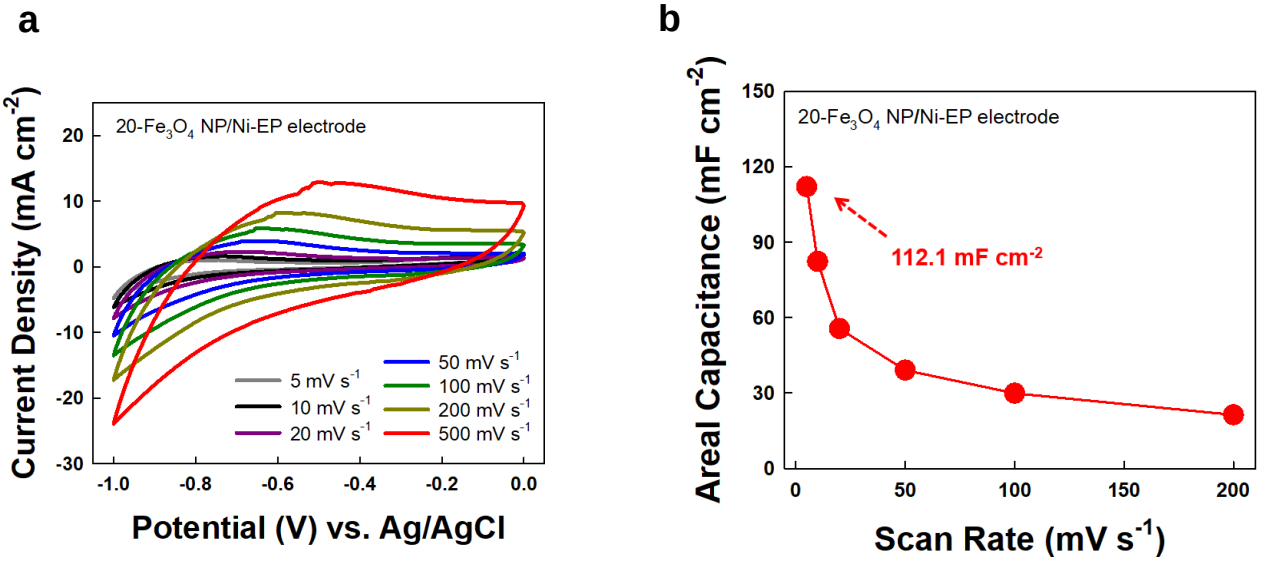

Figure S26. a) CV curves and b) areal capacitances of 20-Fe_3O_4 NP/Ni-EP electrode as a function of scan rate.

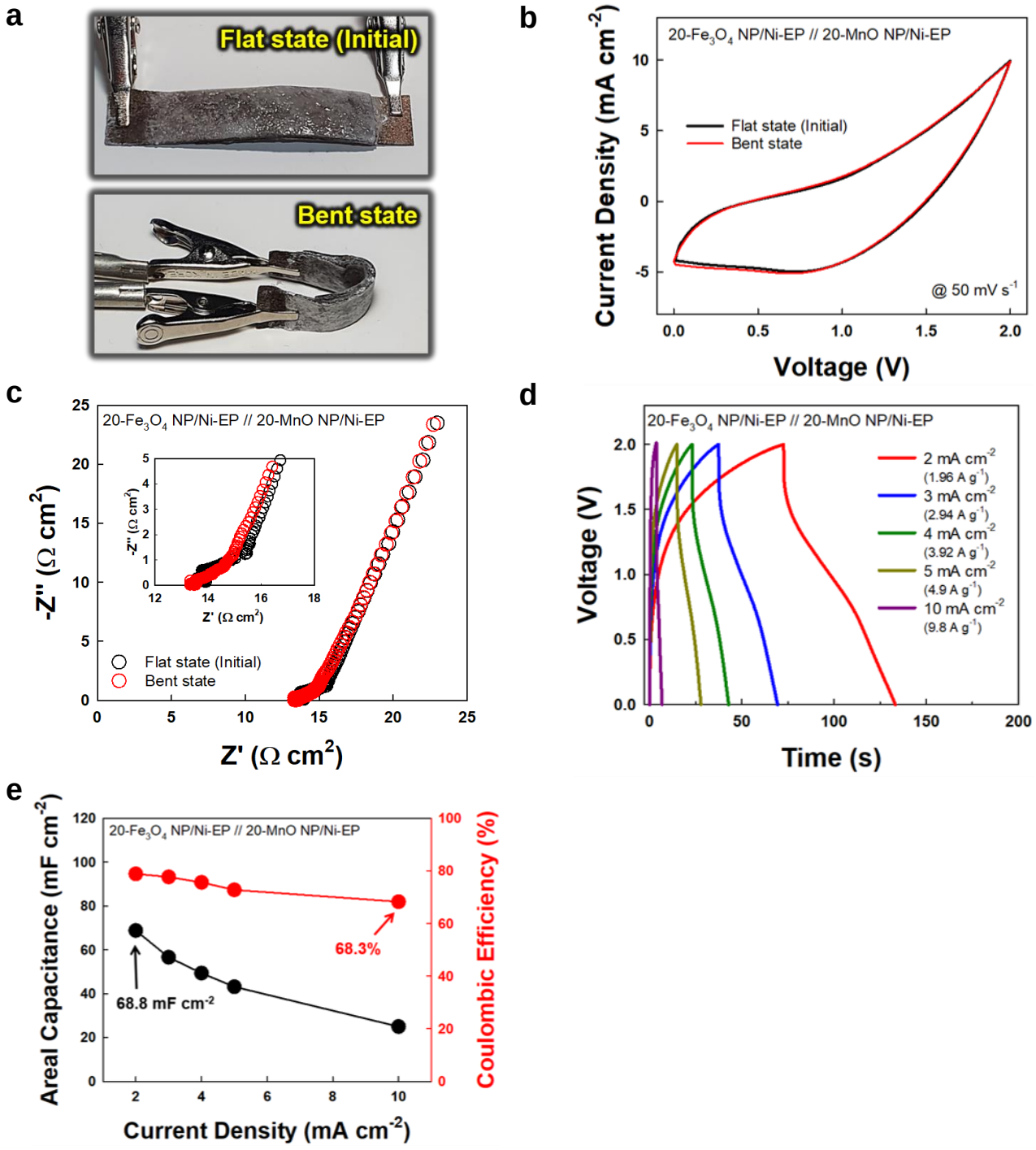

Figure S27. a) Photographic images of the solid-state ASC under flat (initial) and bent state. b) CV and c) Nyquist plots of the solid-state ASC at a scan rate of 50 mV s^{-1} recorded under flat (initial) and bending conditions in the frequency range 100000 Hz to 0.1 Hz, measured at 0.1 V (amplitude potential ~ 5 mV). d) GCD curves, e) areal capacitance, and Coulombic efficiency values of the solid-state ASC at various current densities of 2–10 mA cm^{-2} (0.96–9.8 A g^{-1}).

REFERENCES

[S1] D.A. Buttry, *Marcel Dekker Inc.: New York*, **1991**.

[S2] S. Zhang, N. Pan, *Adv. Energy Mater*. **2015**, *5*, 1401401.